Some considerations on the vibrational environment of the DSC-DCMIX1 experiment onboard ISS

R. Jurado[a], Jna. Gavaldà[a], M. J. Simón[b], J. Pallarés[b], A. Laverón-Simavilla[c], X. Ruiz[a,d], V. Shevtsova[e]

[a] *Dept. Química Física i Inòrganica, Universitat Rovira i Virgili. Tarragona, Spain*
[b] *Departament d'Enginyeria Mecànica, Universitat Rovira i Virgili. Tarragona, Spain*
[c] *E-USOC. ETSIAE, Universidad Politécnica. Madrid. Spain.*
[d] *Institut d'Estudis Espacials de Catalunya. Barcelona. Spain.*
[e] *Department of Chemical Physics. MRC, Univeristé Libre Bruxelles, Brussels, Belgium.*

Abstract

The present work attemps to characterize the accelerometric environment of the DSC-DCMIX1 thermodiffusion experiment carried out in the International Space Station, from November 7th 2011 untill January 16th 2012. Quasi-steady and vibrational/transient data coming from MAMS and SAMS2 sensors have been downloaded from the database of the PIMS NASA website. To be as exhaustive as possible, simultaneous digital signals coming from different SAMS2 sensors located in the Destiny and Columbus modules have also been considered. In order to detect orbital adjustments, dockings, undockings, as well as, quiescent periods, when the experiment runs were active, we have used the quasi-steady eight hours averaged (X_A, Y_A and Z_A) acceleration functions as well as the eight hours RMS ones. To determine the spectral contents of the different signals the Thomson multitaper and Welch methods have been used. On the other hand, to supress the high levels of noise always existing in the raw SAMS2 signals, denosing techniques have been preferred for comparative reboostings considerations. Finally, the RMS values for specific 1/3 octave frequency bands showed that the International Space Station vibratory limit requirements have not been totally accomplished during both quiescent periods and strong disturbances, specially in the low frequency range.

Keywords:

Ternary mixtures, thermodiffusion, DSC-DCMIX1 experiment, International Space Station, ISS

Email address: josepxavier.ruiz@urv.cat (X. Ruiz)

1. Introduction

The accurate determination of the diffusion and thermodiffusion coefficients in ternary liquid systems is a relevant question not only because of its relation with the flow behaviour of the mixture but also because of its implications with the validity of the non-equilibrium thermodynamic matching models of the mixture itself [1, 2]. Due to the very small magnitude of these coefficients, thermal and solutal convective mechanisms in terrestrial laboratories can mask their determination. So, to avoid this masking, experiments as the DCMIX (Diffusion Coefficients in ternary MIXtures) ones are conducted in space platforms, where the gravity is reduced. But, because the own nature of the physical processes implied, molecular diffusion and thermodiffusion experiments take a long time. On Earth laboratories this is not a problem, but in space platforms as the International Space Station, thereafter ISS, the duration of the experiment implies a previous and careful global planning in order to make long enough compatible quiescent intervals with the ISS mandatory daily activities. However, compatibility is sometimes difficult because the ISS is a very active environment. Boostings for orbital adjustments or to avoid collisions with orbital debris, dockings/berthings to bring astronauts/equipment to the ISS, undockings to return the crew to the Earth, flight attitude changes to reorient the ISS to the Sun for power supply reasons, extra vehicular activities for maintenance purposes, crew activities and so on [3, 4, 5, 6].

Due to the importance of the impact of the external environment in any generic liquid experiment, when a large disturbance occurs, such as during Orbital Adjustments (like the Zvezda's ones), the experiment is stopped. The differents experiments were carried out during quiescent periods, in order to prevent possible disturbances on the experiments. Further studies about the impact of the convection in DCMIX experiments are being carried out for the authors, because the related literature does not take into account possible effects of vibrations in the results. The aim of the present work concerns the accurate characterization of the accelerometric quasi-steady and vibratory/transient ISS

environment, focusing on the period when the DSC-DCMIX1 experiment was carried out [7, 8, 9, 10]. This period covers since November 7th 2011 until January 16th 2012. That is to say, the period comprising the installation of the SODI-DSC hardware in the Microgravity Science Glovebox, MSG, in the US-American Destiny laboratory, until the day in which the experiment hardware was finally removed and stowed. The quasi-steady range will give us useful information about the quasi-constant levels attained by large disturbances happened during the experiment while that, the vibratory/transient range will inform us about the spectral characteristics of the mechanical vibrations acting simultaneously. This second range will also check if the environment of the experiment operates accomplishing the ISS vibratory limit requirements or not [11]. Mention here that despite the literature proposes other possible classifications of microaccelerations depending on the inner/outer character of the source or depending on the way of control these microaccelerations [12], the present work uses the common signal frequency classification (quasi-steady and vibratory) because the results presented here are focused on the analysis of the signal itself, regardless the cause that generates it.

The present work constitutes, thus, a first step to a more wide and complete accelerometric characterization of the rest of the DCMIX experiments such as the past DCMIX2 and the near DCMIX3 ones.

2. Digital Signal Processing details

All acceleration data were downloaded from PIMS NASA website [13]. The quasi-steady range is composed by oscillations whose frequencies are lower than 0.01 Hz. Acceleration data in this range, came from the MAMS OSSBTMF accelerometer located in the middeck Lockers 3 and 4 of EXPRESS Rack 1 (ER1), in overhead bay 2 (O2) of the US Laboratory Module (LAB1O2). The vibratory/transient range covers oscillations between 0.01 and 400 Hz. These data came from the MAMS OSS raw sensor also located in the LAB1O2, ER1,

Lockers 3,4 and from the SAMS2 121f08 sensor, at that time near Deck 1 (D1), EXPRESS Rack 3 of the Columbus module (COL1A1, ER3, Seat Track near D1). Also, SAMS 121f02 and 121f03 sensors were at that time located in the U.S. Laboratory. SAMS2 121f02 was mounted in the Microgravity Science Glovebox (LAB1S2, MSG, Upper Left Seat Track) while that SAMS2 121f03 was mounted on the lower Z panel assembly of the EXPRESS Rack 2, in overhead bay 1 (LAB1O1, ER2, Lower Z Panel). Therefore, 121f03 measured directly what the ISS structure was experiencing in terms of vibration while 121f02 measured in contact with the Glovebox. The sample rate of MAMS OSSBTMF and OSS raw are 0.0625 Hz and 10 Hz respectively. The cutoff frequencies are 0.01 and 1 Hz respectively. The 121f02, 121f03 and 121f08 sensors gather data at 1000, 500 and 1000 Hz with cutoff frequencies of 400, 200 and 400 Hz, respectively. Unfortunately, simultaneous data from the Japanese segment of the ISS is not available for comparisons during the different episodes analyzed.

In order to eliminate possible instrument bias we have systematically demeaned all the raw signals before attempting any mathematical manipulation. After the convenient preprocessing of the raw data coming from the different sensors the results presented here are always related to the common ISS Absolute Coordinate System, SSA. Referred to this system the velocity vector is oriented in the same direction as the X-axis and the Z-axis is oriented toward the local vertical (nadir).

Concerning the Power Spectral Density, PSD, mention that the periodogram is not a consistent estimator of its true value. To produce a consistent estimate of it, two different strategies have been used here. The first one is the so-called Welch technique, the second is the Thomson's multitaper method. In summary the Welch technique reduces the variance of the periodogram dividing the time series into segments usually overlapped. Multiplying then each segment by a window function and averaging the set of uncorrelated periodograms obtained a final estimation of the true PSD is made. The Welch method uses, then, the segmenting to decorrelate the different modified periodograms. On the contrary, the Thomson's multitaper method does not consider segments, the method uses

the entire signal and a family of mutually orthogonal windows with optimal time-frequency concentration properties (Slepian sequences) to generate each uncorrelated periodogram [14]. Here, thus, the orthogonality of the Slepian sequences decorrelates the different modified periodograms. To estimate the PSD of the MAMS signals, the Thomson's method has systematically been used, but, for large SAMS2 signals, the Welch method with Hanning windows has been considered more versatile and operative. Mention also that, for convenience, the ordinate scale of the different graphic representations of PSD uses a linear scale for the PSD magnitude in the case Thomson's method (g^2/Hz). In the Welch method the scale is logarithmic (dB/Hz) -although, obviously, both scales are equivalent-.

On the other hand, due to the existence of an important amount of masking noise in all SAMS2 signals, a systematic cleaning process has been carried out before any further comparison. To do so the literature indicates two possible strategies, classical filtering based on Fourier analysis or wavelet denoising using the Discrete Wavelet Transform, DWT [15, 16]. As opposed to a sine and cosine functions used in the Fourier Transform, the DWT decomposes the signal into a set of more versatile basic functions, obtained by dilations and translations of a mother one $\psi(j,k)$. In this way, being $\{x(n), \forall\ n = 0\ ...\ M-1\}$ an initial discrete raw signal- of the space of all square integrable discrete functions, the discrete wavelet reconstruction, $x_{rec}(n)$, of $x(n)$ at level L is given by [17, 18],

$$x_{rec}(n) = \sum_{j=1}^{L} \sum_{k} W_{\psi}(j,k)\psi_{j,k}(n) + \sum_{k} W_{\phi}(1,k)\phi_{1,k}(n) \qquad (1)$$

with $W_{\psi}(j,k)$, $W_{\phi}(1,k)$ the so-called detail and approximation coefficients respectively. The factor $\psi_{j,k}(n)$ is a set of dilations and translations of the mother wavelet $\psi(j,k)$ while that the other one $\phi_{j,k}(n)$ is a set of scale functions, orthogonal to $\psi_{jk}(n)$, used to decompose the generic signal. The scale parameter (dilations) is related with the subindex j while that the temporal displacement (translations) is related with the subindex k.

Equivalently, the discrete wavelet reconstruction, is usually written as,

$$x_{rec} = \sum_{j=1}^{L} D_j + A_L \tag{2}$$

being D_j the detail terms and A_L the approximation one.

The Fast Wavelet Transform algorithm allows the calculation of the different coefficients -and so the different terms- by the use of a diadic filter bank. [19, 20, 21]. This filter bank decomposes the initial broadband of the raw signal into a collection of successively more bandlimited components by repeatedly dividing the frequency range. In wavelet reconstruction only the low-frequency output of the previous level is newly decomposed into adjacent high- and low-frequency subbands by a high- and low-pass filter pair. Each one of the two output subbands is approximately half the bandwidth of the input to that level.

As a consequence of the initial choice of the mother wavelet, the ellimination of noise with these techniques works considerably better than the classical filtering procedures, specially in the case of additive Gaussian white noise in which the noise is spreading in all frequencies [15, 16]. Clearly, if a signal has its energy concentrated in a small number of wavelet dimensions its coefficients will be relatively large compared to the noise which, on the contrary, has its energy spread over a large number of coefficients. This implies that removing the low amplitude values, the reconstructed signal will retrieve a clean signal with little loss of details. To do so, a threshold value λ -or a set of values λ_j- must be considered and compared with every value of the corresponding detail coefficient $W_\psi(j,k)$, in order to decide if this value must be considered as noise or not. Despite there are many possible approaches to the estimation of threshold level we use here a soft thresholding [22]. In this way, this procedure elliminates those coefficients whose absolute values are lower than the corresponding threshold and shrinks the nonzero coefficients toward zero. The denoised signal is finally obtained by adding all the corrected detail terms and the final approximation.

Due to the above-mentioned considerations on the filter effectiveness to ellminate noise, we decide to work here mostly with the discrete wavelet transform. The first step was, thus, the election of a suitable mother wavelet function. In

the present case and after a careful visual approach trying to capture the fine details of the signals we had initially selected three generic orthogonal families, Coiflet, Daubechies and Symlet [17, 18]. In the case of Coiflets we have selected coif2, coif3 and coif4, in the case of Daubechies db3, db4, db5, db6 and db7 and in the case of Symlets sym4, sym6 and sym8. For decomposition levels between one and nine, a quantitative criterion was applied based, for simplicity, on the Percent Root Mean Square of the Difference, PRMSD [23, 24].

$$PRMSD = 100 \cdot \sqrt{\frac{\sum (x_{rec} - x)^2}{\sum x^2}} \tag{3}$$

After that, the DWT decomposes the raw signal into a set of terms, details and a final approximation, enabling the beginning of the denoise process [25, 26]. The present determination of λ employed a procedure based on the minimization of the Stein's Unbiased Risk Estimator, SURE, and a subsequent soft thresholding. However, since this last coefficient represents a low-frequency term containing valuable components of the signal, less affected by the noise, the thresholding [27, 28] here has been restricted to the detail coefficients, not to the approximation one.

Finally, for SAMS2 raw signals, the Root Mean Square (RMS) acceleration levels integrated over each one of the thirty-three one-third octave bands between 0.0891 and 224 Hz, have also been evaluated in order to compare it with the ISS vibratory limit requirements [29, 11]. Hanning windows have been used in all power spectral density calculations [11, 30].

3. Results and Discussion

Table 1 details the most relevant episodes during the DSC-DCMIX1 experiments as well as their origin. The third column gives information about the interval analyzed and the fourth and fith give also information about the sensors used. The number of data is, in all cases, high enough (typically, several hundreds of thousands data each MAMS OSS raw signal and several milions data each SAMS2 signal) to properly describe the different episodes considered.

	Day	Analyzed Interval (UTC)	Analyzed Sensor		Episode type	Origin
			MAMS	SAMS2		
1	09-11-2011	05:07 - 23:00	OSS raw	121f02 121f03	QP	-
2	14-11-2011	-	-	-	SGP	?
3	16-11-2011	-	-	-	DCK	Soyuz TMA-22 (Port: Mini-Research Module 2 -Poisk-)
4	18-11-2011	03:06 - 03:11	OSS raw	-	ZOA	Thruster ignition (Zvezda Service Module)
5	21-11-2011	-	-	-	UDCK	Soyuz TMA-02M (Port: Mini-Research Module 1 -Rassvet-)
6	22-11-2011	-	-	-	SGP	?
7	26-11-201	-	-	-	SGP	?
8	30-11-2011	21:19 - 21:24	OSS raw	-	ZOA	Thruster ignition (Zvezda Service Module)
9	02-12-2011	11:30 - 23:31	OSS raw	-	QP	-
10	09-12-2011	19:50 - 19:51	OSS raw OSSBTMF	121f02 121f03 121f08	ZOA	Thruster ignition (Zvezda Service Module)
11	23-12-2011	-	-	-	DCK	Soyuz TMA-03M (Port: Mini-Research Module 1 -Rassvet-)
12	24-12-2011	13:03 - 23:50	OSS raw	-	QP	-
13	09-01-2012	13:41 - 23:46	OSS raw	-	QP	-
14	13-01-2012	15:18 - 15:23	OSS raw	-	ZOA	Thruster ignition (Zvezda Service Module)

Table 1: Accelerometric episodes all along the DSC-DCMIX1 experiment.**QP**.- Quiescent Period chosen as representative of the different runs; **DCK**.- Docking; **ZOA** Zvezda's Orbital Adjustment (boosting); **UDCK**.- Undocking; **SGP**.- Short Generic Perturbation (unknown origin).

Figure 1 plots the eight hours averaged X_A, Y_A and Z_A quasi-steady acceleration levels and the corresponding RMS values as a function of time, from November 7th 2011 to January 16th 2012. Similarly as the widely used spectrograms [6], this new quasi-steady strategy allows to resume in a few data points –three per day- the evolution of a long time period. Because, in the case of relatively fast events, a resolution of eight hours is very low, the information contained in these kind of graphics is merely indicative. However, sharp changes correlate well with strong disturbances as orbital adjustments. Dockings and undockings can also be detected but their magnitudes are considerably lower [31].

In particular, the information contained in Figure 1 and Table 1 clearly correlates the highest four peaks of the plot (in X_A direction) with the four different Zvezda's Orbital Adjustments, thereafter ZOA. The fact that these disturbances always alter appreciably the X_A values -but not the other Y_A and Z_A ones- shows the high level of directionality of these events. Due to these strong accelerometric impact generated by the ZOA episodes during the DSC-

DCMIX1 experiments, we will pay firstly a special attention on these kind of perturbations. In this respect it is worth mentioning that in the case of the Zvezda Service Module the two main engines, with a thrust of 3070 N each, are reserved for orbital manoeuvring. For ZOAs the 2x16 attitude control engines (with a thrust of 130 N each) were used.

In view of all these preliminar considerations, the following discussion has been divided in two main sections related with the above-mentioned strong disturbances and with quiescent periods, the time periods during the different runs of the experiment take place. In addition, for completness, each section will cover separately two different ranges of frequency, a low (up to 1 Hz) and a high (up to 200/400 Hz) ones This separation is a logical consequence of the two different cutoffs of the MAMS and SAMS2 sensors used.

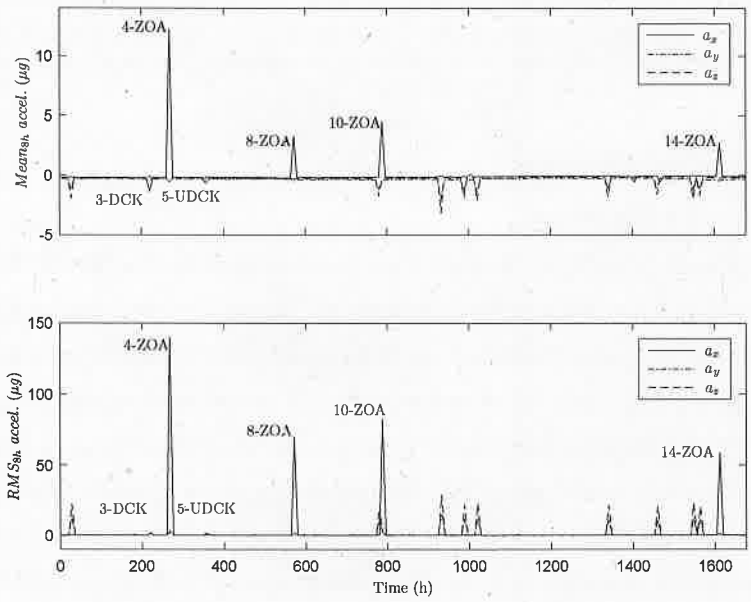

Figure 1: Eight hour averaged X_A, Y_A and Z_A quasy-steady acceleration and RMS values during DSC-DCMIX1 experiment as a function of time, from November 7th 2011 to January 16th 2012.

		Pre-boosting		Bcosting		Post-boosting	
		Freq. range	f_{max}	Freq. range	f_{max}	Freq. range	f_{max}
X_A	4-ZOA	0.177 – 0.185 0.280 – 0.293	0.181* 0.284	0.135 – 0.229	0.176*	0.181 – 0.186	0.184*
	8-ZOA	0.172 – 0.187 0.259 – 0.283 0.599 – 0.630	0.176 0.266 0.616*	0 – 0.355	0.199*	0.175 – 0.183	0.179*
	10-ZOA	0.173 – 0.186 0.272 – 0.281	0.183 0.281*	0.080 – 0.280	0.170*	0.176 – 0.184	0.180*
	14-ZOA	0.183 – 0.169	0.187*	0 – 0.376	0.175*	0.180 – 0.185	0.183*
Y_A	4-ZOA	0.629 – 0.668 0.941 – 0.982	0.648* 0.954	0.141 – 0.229 0.247 – 0.329	0.212* 0.270	0.269 – 0.288 0.380 – 0.398 0.539 – 0.645	0.284 0.393* 0.558
	8-ZOA	0.692 – 0.738 0.808 – 0.859	0.719* 0.837	0.022 – 0.443	0.199*	0.175 – 0.182 0.251 – 0.273 0.832 – 0.852	0.178* 0.270 0.845
	10-ZOA	0.694 – 0.723 0.831 – 0.853	0.709* 0.837	0.010 – 0.798	0.266*	0.175 – 0.182 0.296 – 0.309	0.179* 0.300
	14-ZOA	0.309 – 0.319	0.316*	0.050 – 0.474	0.249*	0.308 – 0.320	0.314*
Z_A	4-ZOA	0.117 – 0.123 0.609 – 0.652	0.121 0.648*	0.076 – 0.229	0.153	0.580 – 0.634	0.597*
	8-ZOA	0.599 – 0.636	0.608*	0.022 – 0.354 0.510 – 0.821	0.111 0.576*	0.606 – 0.614	0.610*
	10-ZOA	0.108 – 0.117 0.599 – 0.639 0.702 – 0.717	0.114 0.623* 0.709	0.080 – 0.292 0.573 – 0.746	0.173 0.639*	0.105 – 0.118 0.609 – 0.659	0.115 0.623*
	14-ZOA	0.117 – 0.124 0.604 – 0.658	0.118* 0.625	0 – 0.740	0.025*	0.117 – 0.124 0.584 – 0.636	0.121 0.620*

Table 2: Significant frequency bands at low frequency for the Pre-boosting, Boosting and Post-boosting analyzed with the MAMS OSS raw sensor. Starred frequencies are the biggest ones.

3.1. Strong disturbances

3.1.1. Low frequencies

The searching of low frequency information have been focused on the interval 0 - 0.01 Hz, the OSS raw's standard cutoff. To do so, we have worked with bands better than with single frequencies because if a certain device creates oscillations of a given frequency, the elements of the ISS as well as the onboard equipment located near this device oscillate with the same or similar frequency. A frequency band is, thus, better suited for the characterization of these oscillations.

To obtain these low frequency bands we firstly calculate the Thomson's periodogram associated with each component of the four ZOAs of DSC-DCMIX1 considering separately the pre-boosting, the boosting and the post-boosting. Then, in each of the thirty-six periodograms analyzed, we select as representative the peak with the highest value of PSD. Bands are then located around all maxima selected in such a way that the bands boundaries correspond the values of frequency which has a magnitude equal to the fifty percent of the

corresponding local maxima. Table 2 details the results obtained in this study. Starred frequencies correspond to frequency values associated with the highest PSD magnitude in the corresponding periodogram. Based on these results it is clear that during the four reboostings of the DSC-DCMIX experiment the spectrum of the X_A component concentrated the maximum values in the interval $0.170 - 0.200\ Hz$. Also, the Y_A component concentrated maxima in the interval $0.210 - 0.270\ Hz$ while that in the Z_A component the results are more scattered. A set of values are located in the interval $0.110 - 0.175\ Hz$ and another single frequencies lower, $0.025\ Hz$, and higher, 0.573 and $0.639\ Hz$ of the above-mentioned interval. On the other hand, pre-boosting results gives frequential characteristics different in the three cartesian axes. In the X_A direction it has been detected intervals located in $0.180 - 0.190\ Hz$ and $0.265 - 0.285\ Hz$. In the Z_A direction the intervals are $0.110 - 0.120\ Hz$ and $0.600 - 0.650\ Hz$ while in the Y_A direction the intervals moved to higher values, $0.645 - 0.720\ Hz$ and $0.835 - 0.845\ Hz$. Post-boosting characteristics are similar to the pre-boostings ones but new single frequencies, 0.179 and $0.558\ Hz$ appears. To illustrate the results compiled in Table 2, Figure 2 shows, as an example, the PSD of the X_A component only -before, during and after a reboosting- for the four ZOAs analyzed. The structural modes of the ISS are located at the low-frequency end of the vibratory range, so, in the present work we will localize them in the range $0.1 - 1\ Hz$. These vibrations, excited by relatively brief impulsive events like a reboost, arise from the excitation of natural frequencies of large components of the structure, for instance the truss or the solar panel arrays. In adition, structural resonances generated by relatively small magnitude vibrations at just the adequate frequencies will also excite these modes. At very low frequencies the ISS can be approximated by a rigid-body, so, structural vibrations propagate via mechanical linkage and arrive throughout the ISS with the same frequencies but different amplitudes depending on the location.

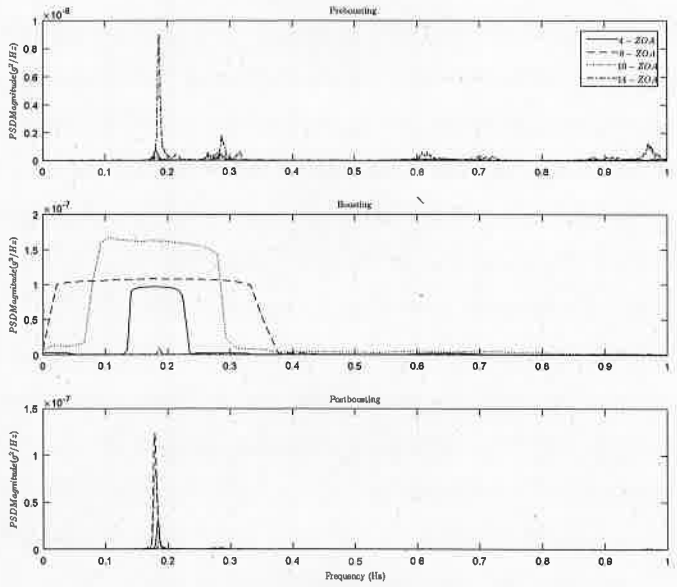

Figure 2: Low frequency spectra in the four ZOAs cases of the X_A acceleration component.

Mention here that none of these bands coincide with the values associated with the elastic vibrations of the ISS and reported in the literature [32]. The denoising process only eliminate the noise, so a possible explanation lies in the fact that the geometry of the ISS before 2012 changed constantly due to the frequent Space Shuttle missions delivering modules (the last Shuttle to the ISS was the STS-135 Atlantis which, docking the ISS on July-10-2011, delivered the Multi-Purpose Logistics Module, Raffaello, to complete the assembly).

3.1.2. High frequencies

Concerning this kind of strong disturbances and because this is the first time that, at the authors advice, a wavelet transformation is introduced in the analysis of SAMS2 data, in this subsection -and only here- we will advance step by step, detailing the procedure used as well as the results obtained. Also, from now on, we will concentrate the characterization on the signal labeled as

10-ZOA in Table 1.

Figure 3 summarizes the calculations effected in the selection procedures of the mother wavelet function in terms of PRMSD coefficient for the three different wavelet families considered. Despite the differences are certainly low and depend more strongly on the particular mother wavelet used than on the level considered, results conclude that the best mother wavelet was sym8 with a detail level L equal to nine.

Figure 4 shows the discrete wavelet decomposition of the raw signal using the selected sym8 wavelet with a detail level equal to nine, $L = 9$. It can be clearly observed that, in the present case, the noise is mainly located in the first four detail terms, D_1 to D_4, and that the last approximation term A_9 maintain the lowest frequency components of the raw signal.

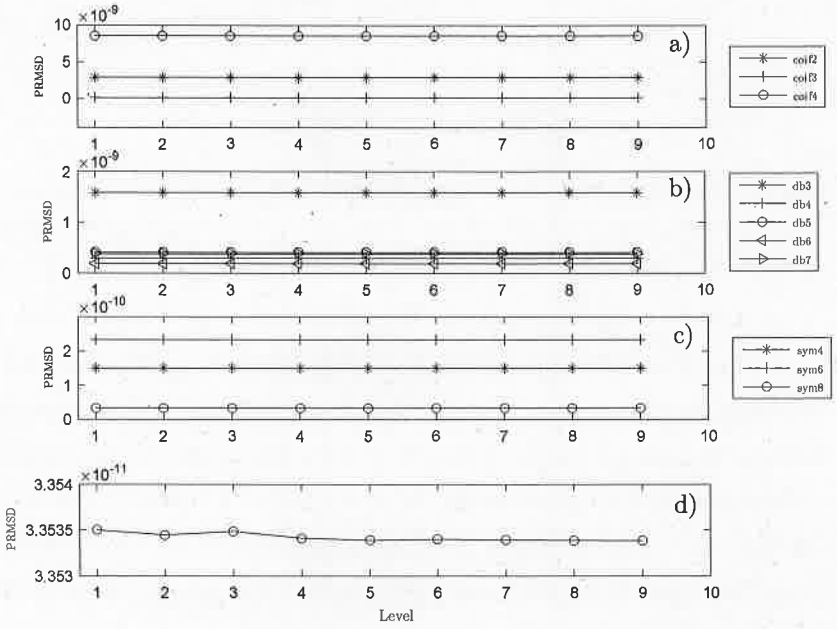

Figure 3: Wavelet selection details from 10-ZOA SAMS2 121f02 in X_A direction. Mother functions: (a) Coiflets, (b) Daubechies, (c) Symlets, and (d) detail of the results only in the sym8 case.

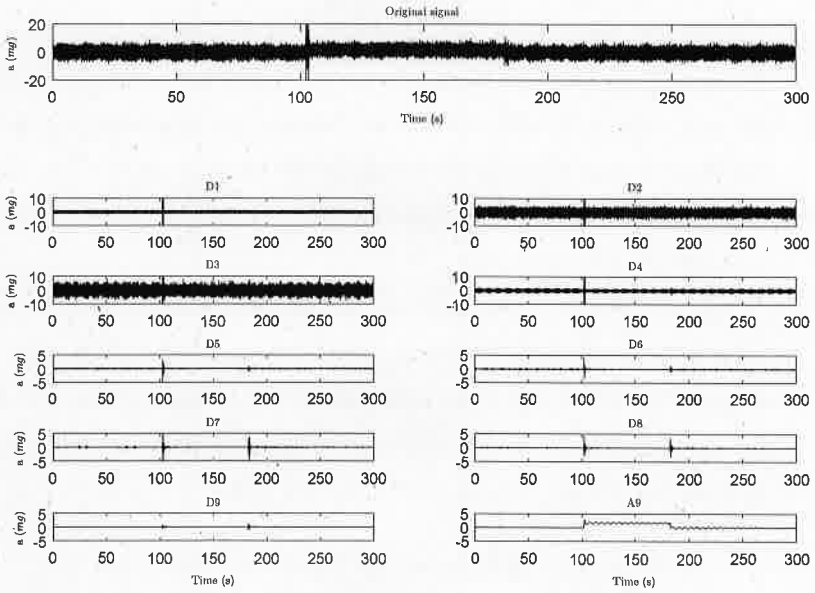

Figure 4: Original raw signal from 10-ZOA SAMS2 121f02 sensor in X_A direction, as well as approximation and detail coefficients until level 9 from its sym8 discrete wavelet decomposition.

Figures 5, 6 and 7 show the same 10-ZOA raw signal together with the PSD, as well as the denoised and the difference ones, respectively. The abrupt features in the original raw signal (see Figure 5) at the begining and the end of the orbital adjustment remain abrupt in the denoised one (see Figure 6). The denoising effect in the frequency domain is drastic, only leaving a few frequencies located in the lower part of the spectrum (see Figure 6). The present denoising strategy is, thus, very effective in the ellimination of high frequency contents of the raw signal as it could be appreciated in Figure 7.

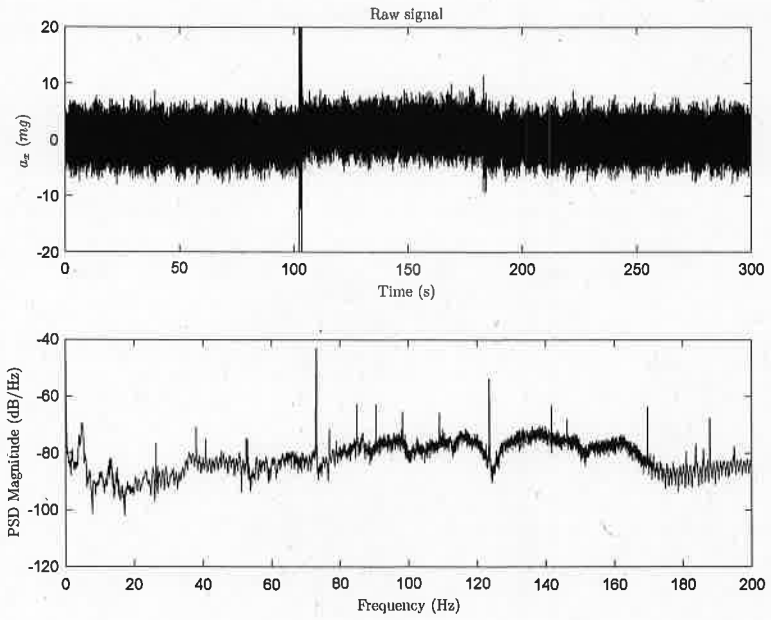

Figure 5: Raw 10-ZOA SAMS2 121f02 signal in X_A direction and Power Spectral Density.

Figure 8 summarizes the different raw MAMS (OSSBTMF and OSS raw) and denoised SAMS2 (121f02, 121f03 and 121f08) 10-ZOA signals in the X_A direction. Remember that OSSBTMF, OSS raw, 121f02 and 121f03 sensors are located in the Destiny module while that 121f08 is located in the Columbus one. As it is shown an average magnitude of about 2 mg is sustained during the 76 s of the ZOA's activity. The onset of the perturbation reasonably agrees in both OSSBTMF and OSS raw cases being the differences simply due to the different sample rates. Concerning the vibrational range it is clear that all denoised signals are very similar to the OSS raw one. The denoising process eliminates higher frequencies and SAMS2 121f02 and 121f03 and 121f08 sensors show a common frequency of roughly 0.2 Hz. Figures 9 and 10 summarize the components of Y_A and Z_A. Both the quasi-steady and vibratory/transient values are considerably lower than the X_A ones. Y_A component have the same shape as Z_A, but with lower magnitude except for signals coming from the

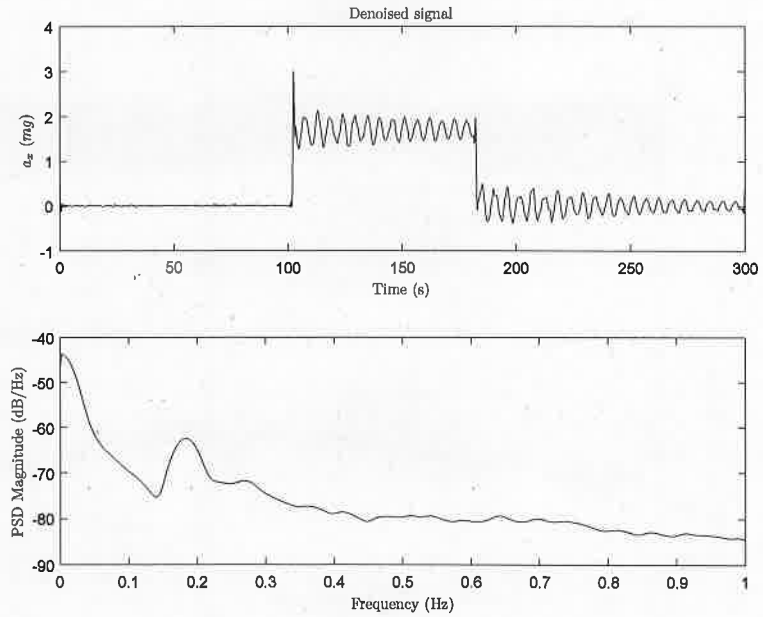

Figure 6: Denoised 10-ZOA SAMS2 121f02 signal in X_A direction and Welch's Power Spectral Density.

Columbus module, which have the same intensity. Also, in both Y_A and Z_A components, SAMS2 121f02 and 121f03 sensors (cases *b* and *c*), register a lower amplitude than the 121f08 one (cases *d* in Figures 9 and 10). Remark finally the fact that only SAMS2 data enable to investigate the low frequency contents of the different signals not only from the Destiny module but also from the Columbus and Kibo ones. There are no MAMS sensors in the above-mentioned two modules.

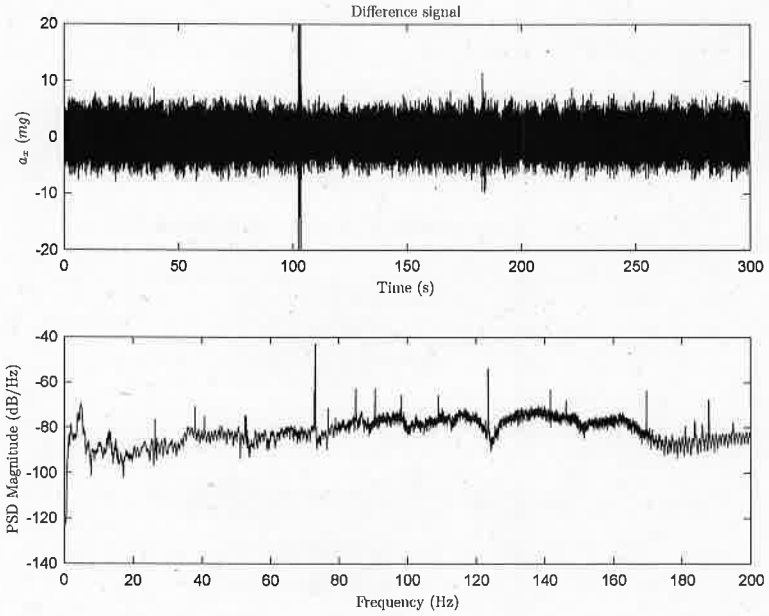

Figure 7: Difference 10-ZOA SAMS2 121f02 signal in X_A direction and Welch's Power Spectral Density.

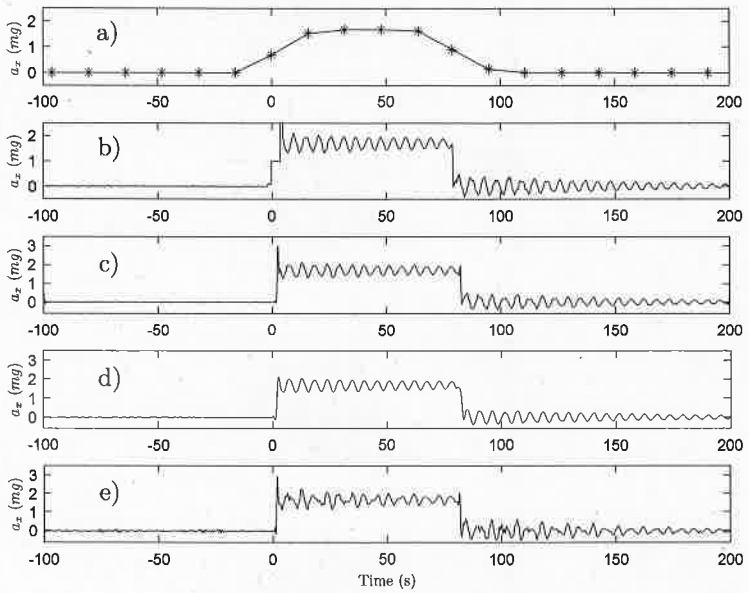

Figure 8: Quasi-steady and vibratory/transient 10-ZOA X_A signals coming from: (a) OSS-BTMF and (b) OSS raw sensors. Denoised signals from: (c) 121f02, (d) 121f03 and (e) 121f08 sensors are also plotted.

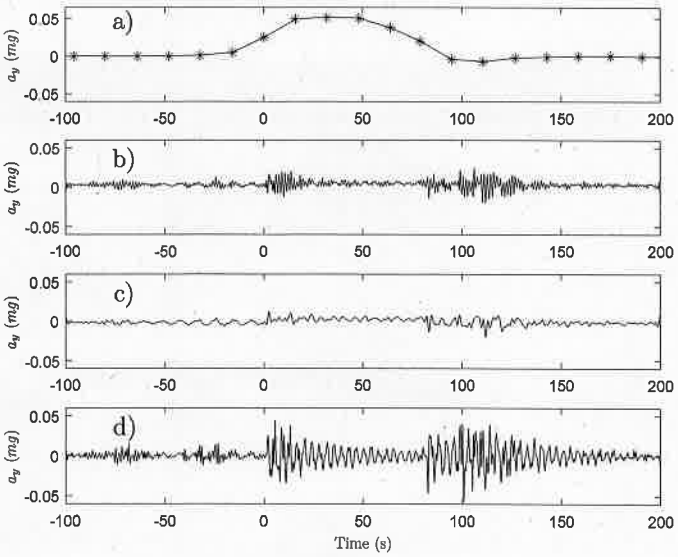

Figure 9: Quasi-steady and vibratory/transient 10-ZOA Y_A signals coming from: (a) OSS-BTMF. Denoised signals from: (b) 121f02, (c) 121f03 and (d) 121f08 sensors are also plotted.

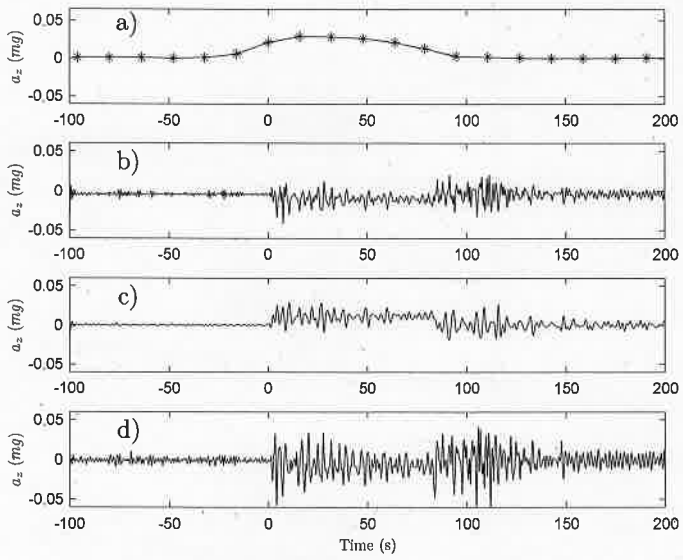

Figure 10: Quasi-steady and vibratory/transient 10-ZOA Z_A signals coming from: (a) OSS-BTMF. Denoised signals from: (b) 121f02, (c) 121f03 and (d) 121f08 sensors are also plotted.

Finally, Figure 11 compares the RMS values for specific one third octave frequency bands of SAMS2 121f02, 121f03 and 121f08 against the ISS vibratory limit requirements before and during the 10-ZOA big disturbance. The figure shows also the low frequency range because the used signal have been obtained with the SAMS2 sensor. Although all sensors have similar spectral features for the medium frequency range during ZOAs, the RMS level in the low frequency range ($< 1\ Hz$ approximately), increases considerably during the reboosting episode. In all cases the limits are largely exceed. Before the reboost, the low frequency levels of the signals coming from the SAMS2 121f02 and 121f03 sensors also exceed sligthly the limits required. The Destiny SAMS2 121f02 and 121f03 signals show several increases in the bands containing the frequencies associated with air processing machinery. Mention finally that the localization of the sensor inside the Glovebox (121f02) or in contact with the structure itself

(121f03) introduces significative changes in the signals mainly at the higher frequencies.

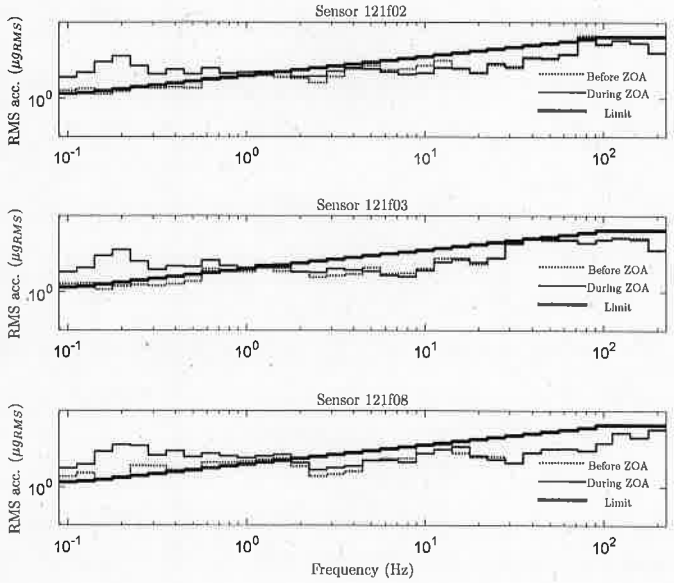

Figure 11: SAMS2 121f02-121f03-121f08 (Destiny-Destiny-Columbus) 10-ZOA RMS acceleration values vs. the ISS vibratory limit requirements.

3.2. Quiescent periods

3.2.1. Low frequencies

As before, the searching for low frequency bands in the raw MAMS OSS raw quiescent periods have been focused on the segment 0 - 1.0 Hz.

Figure 12 shows that the most significant band for the X_A component is in all cases located at $0.176 - 0.195$ Hz. It has been detected that, for frequencies higher than 0.3 Hz and lower than 0.15 Hz, the PSD magnitude is very low. So, Figure 12 concentrates in the $0.15 - 0.3$ Hz interval. The frequency of the dominant peak in this band is 0.185 Hz, approximately. Concerning the Y_A components, the coincidence between bands for the four different signals con-

		Freq. range	f_{max}
X_A	1-QP	$0.179 - 0.195$	0.1898^*
	9-QP	$0.176 - 0.198$	0.1845^*
		$0.264 - 0.280$	0.2711
	12-QP	$0.179 - 0.197$	0.1833^*
		$0.267 - 0.280$	0.2737
	13-QP	$0.181 - 0.208$	0.1862^*
		$0.268 - 0.277$	0.2741
Y_A	1-QP	$0.121 - 0.144$	0.1267^*
		$0.610 - 0.656$	0.6420
	9-QP	$0.097 - 0.114$	0.1012
		$0.578 - 0.669$	0.6127^*
	12-QP	$0.089 - 0.118$	0.1058
		$0.255 - 0.275$	0.2580
		$0.547 - 0.676$	0.6055^*
	13-QP	$0.095 - 0.108$	0.0976
		$0.250 - 0.281$	0.2579
		$0.555 - 0.740$	0.6026^*
Z_A	1-QP	$0.262 - 0.341$	0.3199^*
		$0.406 - 0.423$	0.4087
	9-QP	$0.236 - 0.334$	0.3171^*
		$0.391 - 0.415$	0.4118
	12-QP	$0.255 - 0.276$	0.2591
		$0.299 - 0.326$	0.3093^*
	13-QP	$0.260 - 0.366$	0.3155^*
		$0.560 - 0.569$	0.5685

Table 3: Significant frequency bands at low frequency for the four Quiescent Periods (1-QP, 9-QP, 12-QP and 13-QP) analyzed with the MAMS OSS raw sensor.

sidered is not as good as in the X_A case, but they still have common frequency bands located at $0.095 - 0.144\ Hz$, and $0.547 - 0.740\ Hz$, which have two associated peaks at 0.127 and 0.613 Hz respectively, and their amplitudes are greater than the one associated with the X_A component. In the case of Z_A component a common interval between $0.255 - 0.321\ Hz$ is also detected. Table 3 details all data used for the obtaining of these common bands. Notice that the band $0.176 - 0.195\ Hz$ of the X_A component also appears during reboostings. This seems to suggest, again, that despite the disagreement with the values published in the literature [32], this low frequency band could be correlated with structural vibrations of the ISS. Concerning the other two Y_A and Z_A directions, there is no common bands if comparing reboostings results of Table 2.

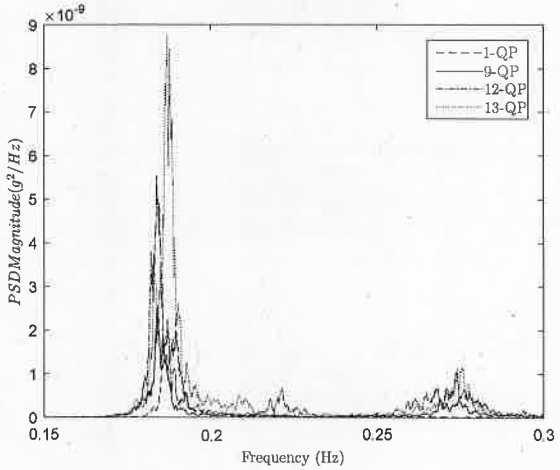

Figure 12: Thomson's Power Spectral densities of the four X_A components corresponding to 1-QP, 9-QP, 12-QP and 13-QP MAMS OSS raw signals.

3.2.2. High frequencies

As typical examples of quiescent periods in the vibrational/transient range Figure 13 shows two raw signals of 1-QP coming from the SAMS2 121f02 and 121f03 sensors located in the Glovebox and in the lower Z panel respectively. Unfortunately, Columbus module signals from 121f08 were not available that day.

At this respect, it is interesting to mention that the 121f03 signal (structure) is noisier than the 121f02 one (Glovebox). The structure receive vibration from the whole ISS, therefore, the noise level is higher. The Glovebox's devices cause sudden peaks in the signal, but the level of noise is lower due to the isolation on the structure.

The denoise procedure applied to these couple of signals also eliminates their high frequency contents (see Figure 14). However, now the results are not as relevant as in the previous section. In fact, this procedure does not discover any peculiar trend to be compared. So, we will use all raw SAMS2 signals for further discussions here.

Label Table 1	Sensor	Frequency Peak (X_A) (Hz)	Frequency Peak (Y_A) (Hz)	Frequency Peak (Z_A) (Hz)
1 - QP	121f02	141.7	73.1	98.26
	121f03	141.7	141.7	98.26
9 - QP	121f02	73.1	73.1	73.1
	121f03	141.7	141.7	141.7
12 - QP	121f02	141.7	98.26	98.26
	121f03	141.7	141.7	141.7
13 - QP	121f02	90.55	73.1	73.1
	121f03	141.7	141.7	141.7

Table 4: Spectral characteristics of the raw signals during the four Quiescent Periods (1-QP, 9-QP, 12-QP and 13-QP) in the vibrational/transient range.

The spectral study of the SAMS2 signals have been focused on the segments 1 - $400Hz$ and 1 - $200Hz$ respectively due to the different cutoff values of both the 121f02 and 121f03 SAMS2 signals. Concerning the 121f02 sensor, inside the Glovebox, the dominant frequencies are 73.11 Hz, 90.56 Hz and 289.2 Hz (see Table 4). All these high values are related with machinery. For instance, 98.26 Hz could be related with Common Cabin Air Assembly while that the 73 Hz peak could be attributed, as mentioned before, to the Glovebox fan in open mode [6]. The spectral fingerprint of the 121f03 sensor is similar. The dominant frequency in practically all cases is located at 141.7 Hz, which corresponds to the Intermodule Ventilation (IMV) fan. In other words, high frequency analyses of the quiescent periods are mainly dominated by the activity of air processing machinery. However elliminating the frequency values associated with these stronger amplitudes, the low frequency contents are very similar to the ones reported in the previous subsection.

Finally, Figure 15 also presents the RMS acceleration values for two raw signals during 1-QP. The figure shows also the low frequency range because the used signal have been obtained with the SAMS2 sensor. It can be seen, that in all octave bands the amplitudes are lower than the corresponding ISS requirement limits for the case of the Glovebox 121f02 sensor. These limits are excedeed in certain bands for the 121f03 sensor located in contact with the ISS structure. Mention also that, 121f03 RMS values are greater than 121f02 ones at low and high frequencies.

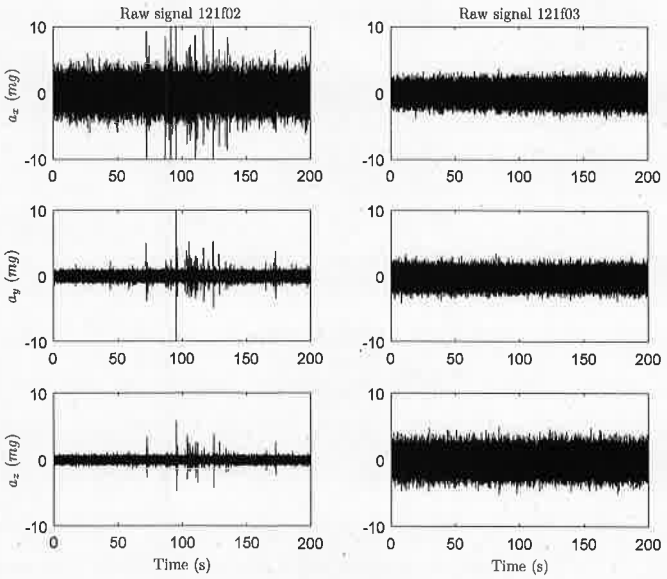

Figure 13: Raw 1-QP signals during a quiescent period from SAMS2 121f02 and 121f03 sensors in X_A, Y_A and Z_A directions.

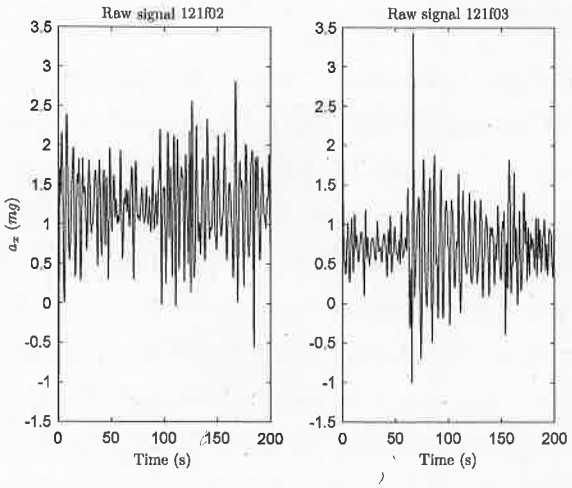

Figure 14: Denoised 1-QP signals during a quiescent period from SAMS2 121f02 and 121f03 sensors in X_A directions.

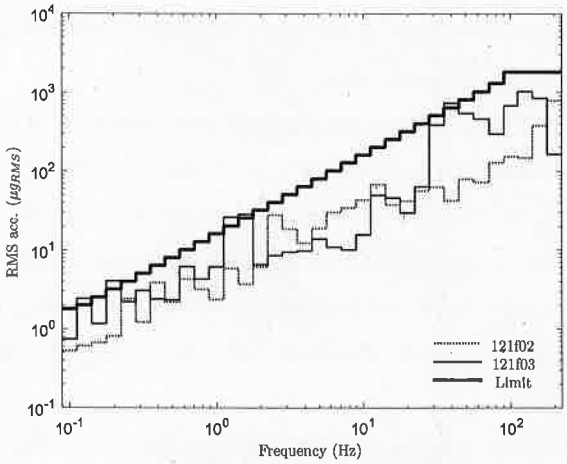

Figure 15: 1-QP RMS values from SAMS2 121f02-121f03 (Glovebox-Lower Z panel) vs the ISS vibratory limit requirements.

4. Conclusions

The acceleration environment of the DSC-DCMIX1 experiment in both quasi-steady and vibrational/transient ranges has been analyzed here.

The eight hours averaged X_A, Y_A and Z_A acceleration levels as a function of time, are used here as detector of the main disturbances existing during DCMIX1 experiments. Although with some restriction against fast perturbation with characteristic time lower than eight hours, these signals correlate well with the different strong disturbances that occurred all along the experiments. On the other hand, emphasize also that the comparative analysis done with the noisy SAMS2 raw signals has been based on the discrete wavelet transform (denosing technique). After some preliminary considerations concerning the particular wavelet to be used as well as its level, the present results show that the application of this technique offers good results in the ellimination of the high frequency component of the SAMS2 raw signals. So, the denoising technique enable clear and fast comparisons of the different SAMS2 signals, mainly during the four reboosting episodes. In the case of quiescent periods this procedure does not add any additional advantage.

During the strong ZOAs disturbances, low frequency bands are different for the three Cartesian coordinates and in the X_A direction -the reboosting direction- the most representative frequencies are in between 0.170 and $0.199 Hz$. At high frequencies, the denoising of SAMS2 data discover similar patterns in all cases. On the other hand, during strong ZOAs disturbances the environment did not accomplish the ISS vibratory limits requirements, mainly in the low frequency range.

During quiescent periods, the low frequency bands are different for the three Cartesian components, but all have, at least, one band comprising frequencies lower than 0.35 Hz. The origin of these bands is not clear, but according to the literature it seems that they are apparently structural [32]. High frequency spectra show very intense peaks associated with air processing machinery. These peaks are the responsible that the octave bands containing their values are

slightly higher than the ISS vibratory limits requirements. The accelerometer at the Glovebox is within the required limits, while the sensor attached to the structure of the experimental module is slighty higher.

Acknowledgements

We acknowledge the constant support offered by Dr. K. Hrovat (ZIN Technologies, Inc.). The present work has been supported by grants ESP2014-53603-P from the Spanish Ministerio de Economía y Competitividad, MINECO, 2014SGR365 of the Generalitat de Catalunya. J. Pallarés acknowledges funding from project CTQ2013-46799-C2-1-P (MINECO).

References

[1] M. Rahman, M. Z. Saghir, Thermodiffusion or soret effect: Historical review, International Journal of Heat and Mass Transfer 73 (2014) 693–705.

[2] S. Srinivasan, M. Saghir, Thermodiffusion in multicomponent mixtures, Springer, 2013.

[3] E. Ceglia, European users guide to low gravity platforms, Erasmus, 2005.

[4] K. McPherson, E. Kelly, J. Keller, Acceleration environment of the international space station, in: AIAA Aerospace Sciences Meeting Including The New Horizons Forum and Aerospace Exposition, Vol. 0957, AIAA, 2009, pp. 953–958.

[5] Reference guide to the international space station, 2010.

[6] NASA, Pims nasa handbook (2013).
URL `http://pims.grc.nasa.gov/pimsdocs/public/ISS%20Handbook/hb_vib_equipment_MSG_Operations.pdf`

[7] S. Van Vaerenbergh, J. C. Legros, J. L. Daridon, T. Karapantsios, M. Kostoglou, Z. Saghir, Multicomponent transport studies of crude oils and asphaltenes in dsc program, Microgravity-Science and Technology 18 (3-4) (2006) 150–154.

[8] A. Ahadi, M. Z. Saghir, Contribution to the benchmark for ternary mixtures: Transient analysis in microgravity conditions, The European Physical Journal E 38 (4) (2015) 1–10.

[9] A. Ahadi, M. Z. Saghir, The microgravity DSC-DCMIX1 mission onboard iss: Experiment description and results on the measurement of the soret coefficients for isobutylbenzene, dodecane, tetralin ternary hydrocarbons mixtures, Experimental Thermal and Fluid Science 74 (2016) 296–307.

[10] V. Sechenyh, J. C. Legros, A. Mialdum, J. O. de Zárate, V. Shevtsova, Fickian diffusion in ternary mixtures composed by 1,2,3,4-tetrahydronaphtalene, isobutylbenzene and n- dodecane, The Joiurnal of Physical Chemistry B 120 (2016) 535–548.

[11] N. Sáez, X. Ruiz, J. Gavaldà, V. Shevtsova, Comparative analyses of ESA, NASA and JAXA signals of acceleration during the SODI-IVIDIL experiment, Microgravity Science and Technology 26 (1) (2014) 57–64.

[12] A. Sedelnikov, Classification of microaccelerations according to methods of their control, Microgravity Science and Technology 27 (2015) 245–251.

[13] NASA, Pims nasa website.
URL `http://pims.grc.nasa.gov/html/ISSAccelerationArchive.html`

[14] D. Percival, A. T. Walden, Spectral Analysis for Physical Applications: Multitaper and Conventional Univariate Techniques, Cambridge University Press, 1993.

[15] B. Shenoi, Introduction to digital signal processing and filter design, John Wiley & Sons, 2005.

[16] S. V. Vaseghi, Advanced digital signal processing and noise reduction, John Wiley & Sons, 2008.

[17] D. Percival, A. Walden, Wavelet methods for time series analysis, Vol. 4, Cambridge university press, 2006.

[18] N. Goswami, C. Jaideva, A. Chan, Fundamentals of wavelets: theory, algorithms, and applications, Vol. 233, John Wiley & Sons, 2011.

[19] K. Shukla, A. Tiwari, Efficient Algorithms for Discrete Wavelet Transform with Applications to Denoisisng and Fuzzy Inference Systems, Springer, 2013.

[20] S. Mallat, A wavelet tour of signal processing: the sparse way, Academic press, 2008.

[21] I. Daubechies, Ten lectures on wavelets, SIAM, 1992.

[22] B. Ergen, Comparison of wavelet types and thresholding methods on wavelet based denoisingof heart sounds, Journal of Signal and Information Processing 4 (2013) 164–167.

[23] Y. Chompusri, K. Dejhan, S. Yimman, Mother wavelet selecting method for selective mapping technique ecg compression, in: Electrical Engineering/Electronics, Computer, Telecommunications and Information Technology (ECTI-CON), 2012 9th International Conference on, IEEE, 2012, pp. 1–4.

[24] W. K. Ngui, M. S. Leong, L. M. Hee, A. Abdelrhman, Wavelet analysis: mother wavelet selection methods, in: Applied mechanics and materials, Vol. 393, Trans Tech Publ, 2013, pp. 953–958.

[25] D. Donoho, I. Johnstone, Adapting to unknown smoothness via wavelet shrinkage, Journal of the american statistical association 90 (432) (1995) 1200–1224.

[26] M. Kania, M. Fereniec, R. Maniewski, Wavelet denoising for multi-lead high resolution ecg signals, Measurement science review 7 (2007) 30–33.

[27] C. M. Stein, Estimation of the mean of a multivariate normal distribution, The annals of Statistics (1981) 1135–1151.

[28] E. Candes, C. A. Sing-Long, J. D. Trzasko, Unbiased risk estimates for singular value thresholding and spectral estimators, Signal Processing, IEEE Transactions on 61 (19) (2013) 4643–4657.

[29] N. Sáez, X. Ruiz, J. Gavalda, J. Pallares, V. Shevtsova, Comparative ISS accelerometric analyses, Acta Astrnautica 94 (2014) 681–689.

[30] M. Rogers, K. Hrovat, K. McPherson, M. Moskowitz, T. Reckart, Accelerometer data analysis and presentation techniques, NASA Technical Report.

[31] N. Sáez, X. Ruiz, M. Pujalte, J. Gavaldà, On the detection of external disturbances using reduced quasi-steady accelerometric data, in: ELGRA Biennial Symposium and General Assembly, 2013.

[32] D. Zavalishin, M. Y. Belyaev, V. Sazonov, Study of vibration microaccelerations, Cosmic Resarch 51 (4) (2013) 261–269.